Journal of Materials Chemistry A

ROYAL SOCIETY OF CHEMISTRY

PAPER

View Article Online
View Journal

Cite this: DOI: 10.1039/d5ta03069b

Machine learning-assisted optimization design for enhanced oxygen evolution reaction based on vanadium-doped nickel–cobalt layered double hydroxides†

Chandrasekaran Pitchai, ‡[a] Ting-Yu Lo, ‡[a] Hou-Chien Chang, [a] Hung-Chung Li, *[be] Ming-Der Yang *[cde] and Chih-Ming Chen *[ade]

The increasing demand for sustainable energy has driven significant research into efficient water splitting, particularly the development of electrocatalysts for the oxygen evolution reaction (OER) which is limited by sluggish kinetics. Optimization of the OER process remains, however, a big challenge due to the compositional complexity of multicomponent catalysts and the influences of electrolyte and temperature. In this study, machine learning (ML)-assisted optimization design is performed to enhance the OER performance using vanadium-doped nickel–cobalt layered double hydroxides (NiCoV LDHs) as the catalyst. In the ML framework, a polynomial regression model is systematically trained by experimental datasets to successfully elucidate the correlation between the target feature (overpotential) and the input features (catalyst composition, electrolyte concentration, and reaction temperature) with a high coefficient of determination (R^2) of 0.842. Based on the optimized input features predicted by the ML algorithm, a superior overpotential of 196 mV is experimentally obtained which is reduced by 21% compared to the best catalytic performance (238 mV) in the original training datasets. Structural and electrochemical characterizations confirm a well-defined layered morphology and efficient charge transfer dynamics for the optimized electrocatalyst. Our results stand as a significant milestone for integrating an ML algorithm with experimental synthesis for the rational design and optimization of high-performance, cost-effective OER electrocatalysts.

Received 18th April 2025
Accepted 22nd June 2025

DOI: 10.1039/d5ta03069b

rsc.li/materials-a

1 Introduction

In recent decades, rapid population growth and technological advancements have driven a surge in energy consumption, highlighting the limitations of fossil fuels and the pressing environmental challenges.[1–4] This has sparked widespread research into renewable and eco-friendly energy alternatives, with hydrogen emerging as a key focus. The fields of energy conversion and storage have seen rapid advancements, with hydrogen emerging as a leading contender for future energy solutions due to its clean nature, high energy density, recyclability, and abundant availability.[5–7] Eco-friendly characteristics and cost-effective production methods, particularly through electrochemical processes, make hydrogen an increasingly attractive option. Building on the importance of electrochemical hydrogen production, water splitting in an electrolyzer plays a vital role in sustainable energy systems. It is essential for green hydrogen generation and involves two key half-reactions: the hydrogen evolution reaction (HER) and the oxygen evolution reaction (OER).[8–10] This process necessitates a higher overpotential (1.8–2 V *vs.* SHE) than the theoretical minimum (1.23 V *vs.* SHE) due to intrinsic reaction barriers.[11] Noble metals such as Pt, Ru, Ir, and Au have shown exceptional performance in reducing overpotential, with Pt and Ru/Ir oxides being particularly effective in minimizing energy losses at the cathode and anode.[12] In particular, the OER involves complex reaction mechanisms with multiple catalytic steps, resulting in sluggish electrochemical kinetics, and is a complex four-electron transfer process requiring substantial additional potential.[13,14] Addressing these kinetic challenges is critical, as the OER significantly impacts the overall efficiency of energy

[a]Department of Chemical Engineering, National Chung Hsing University, Taichung 402202, Taiwan. E-mail: chencm@nchu.edu.tw; Tel: +886-4-22840510 ext.511

[b]Undergraduate Program of Intellectual Creativity Engineering, National Chung Hsing University, Taichung 402202, Taiwan. E-mail: hcli01@nchu.edu.tw; Tel: +886-4-22840430 ext.702

[c]Department of Civil Engineering, National Chung Hsing University, Taichung 402202, Taiwan. E-mail: mdyang@nchu.edu.tw

[d]Innovation and Development Center of Sustainable Agriculture, National Chung Hsing University, Taichung 402202, Taiwan

[e]Smart Sustainable New Agriculture Research Center (SMARTer), National Chung Hsing University, Taichung 402202, Taiwan

† Electronic supplementary information (ESI) available. See DOI: https://doi.org/10.1039/d5ta03069b

‡ These authors have equal contribution.

production and storage systems. Developing advanced, cost-effective electrocatalysts is essential to overcome these limitations, facilitating faster reaction rates and enhancing the overall water splitting process.[15–18]

Recent studies have increasingly highlighted the potential of hydroxide-based catalysts, particularly layered double hydroxides (LDHs) with their distinctive stratified architectures, for promoting the OER under alkaline conditions.[19] Transition metal-based LDHs such as CoFe-LDHs, NiCo-LDHs, and NiFe-LDHs have demonstrated notable OER performance.[20,21] However, challenges remain, especially with NiCo-LDHs, which often suffers from inadequate long-term electrocatalytic stability. This decline in activity is largely due to unavoidable aggregation and restacking of its nanosheets, in addition to its inherently low electrical conductivity and overall stability. To address these limitations, researchers have explored doping strategies; incorporating one or more foreign cations into these bimetallic hydroxides has proven effective in significantly enhancing OER kinetics by tuning both their electronic properties and structural resilience.[22]

Vanadium (V) doping in $FeNi_3N/Ni_3N$ results in an overpotential of 230 mV, compared to 244 mV for the undoped counterpart. This improvement in OER kinetics can be attributed to the electronic modifications occurring at the interface between the two nitride phases due to vanadium incorporation.[23] Similarly, He *et al.* modified sheet-like Ni_3Se_2 through vanadium doping, which significantly altered the selenide structure and enhanced its OER performance, achieving an overpotential of just 270 mV.[24] Additionally, Bera and colleagues synthesized V-doped NiCo LDHs *via* a co-precipitation method and demonstrated its effectiveness as an electrocatalyst for OER. Their catalyst reached a current density of 10 mA cm^{-2} at an overpotential of 280 mV, accompanied by an impressively low Tafel slope of 67 mV dec^{-1}.[22]

Machine learning (ML), as a key technology to implement artificial intelligence, has become an emerging tool for optimal performance prediction through dataset analysis and model.[25–30] In recent years, ML has been used as a screening tool of efficient electrocatalysts for hydrogen production.[31–34] Cao *et al.* used ML to screen specific transition metals (TM) doped metal phosphides as potentially active HER catalysts.[35] In their study, density functional theory (DFT) was used to construct the adsorption energy of HER intermediates and critical catalyst features, *e.g.* local average electronegativity, as the ML dataset. Zhou *et al.* reported a similar methodology for the design of TM-doped covalent organic frameworks (COFs) as efficient OER catalysts.[36] The DFT calculation method was used to acquire the dataset of the free energy required for the four-electron transfer pathway toward the OER for all catalysts of interest.[37] Although the DFT-based ML screening methodology is time and cost effective, its prediction accuracy still needs further experimental evidences. Besides, the DFT calculation merely considers the influence of the structures and compositions of the catalysts, rarely emphasizing the influence of other features such as synthesis temperature and electrolyte concentration. Noteworthy, the interplay between synthesis temperature/electrolyte concentration and catalysts plays a vital role in the OER and HER.[38–40]

The generation of initial dataset is the key first step to drive the ML technology. Collecting experimental data from different literature sources is an approach commonly used to generate the dataset.[41,42] However, the sources of experimental data are relatively scattered, and there may be differences in the catalyst synthesis methods, resulting in high incompleteness and uncertainty of the collected data, which seriously affects the training results of ML. In this study, TM-based NiCoV LDHs were used as the electrocatalyst of the OER and the initial dataset was generated experimentally with the catalyst composition, synthesis temperature, and electrolyte concentration as the feature variables. Thirty-five sets of feature variables were randomly selected within a specific framework as the process conditions of the OER, which also produced thirty-five sets of experimental data as the training dataset of ML. Subsequently, ML optimization was performed to systematically investigate the influences of four critical features on the electrocatalyst performance. Based on the ML results, the optimized catalyst was synthesized, demonstrating significantly improved OER performance with a low overpotential of 196 mV and Tafel slope of 102.8 mV dec^{-1}. A minor deviation of 6.1% from the predicted overpotential of 185 mV shows that the ML framework used in this study is a useful tool for the rational design of more efficient catalysts for alkaline OER applications.

2 Results and discussion

2.1. Generation of training dataset by experiments

TM-based NiCoV LDHs electrocatalysts and their electrochemical performance of OER, that is, the overpotential required to reach a current density of 10 mA cm^{-2} were systematically evaluated using ML. The catalyst composition, synthesis temperature, and electrolyte concentration were used as the feature variables to experimentally synthesize the catalysts, and the synthesized catalysts were evaluated to acquire the overpotential for the OER. Thirty-five sets of experimental data were generated according to the ranges of feature variables in Table S1 (ESI)† and used as the initial training dataset for ML. In Table S1,† the catalyst composition includes Ni, Co, and V. The compositions of the two transition metals, Ni and Co, were the same, ranging from 0.35 to 0.45, and that of the V dopant ranged from 0.1 to 0.3. The temperature used for the catalyst synthesis was set in the range of 150 °C to 200 °C, and the concentrations of the electrolyte (KOH) and urea were from 0.1 M to 1 M and 5.83 mM to 7.43 mM, respectively. The electrochemical activity of all synthesized NiCoV LDHs coated on the nickel foam (NF) electrode was investigated through linear sweep voltammetry (LSV) with a scan rate of 10 mV s^{-1}. Based on the LSV curves in Fig. S1 (ESI),† the overpotential data required to reach a current density of 10 mA cm^{-2} were found to be in the range of 238 mV to 361 mV as shown in Fig. S2(a).†

2.2. Optimization of synthesis parameters by machine learning

Fig. 1 illustrates the complete ML optimization process, and Fig. 2 illustrates the feature engineering and selection for

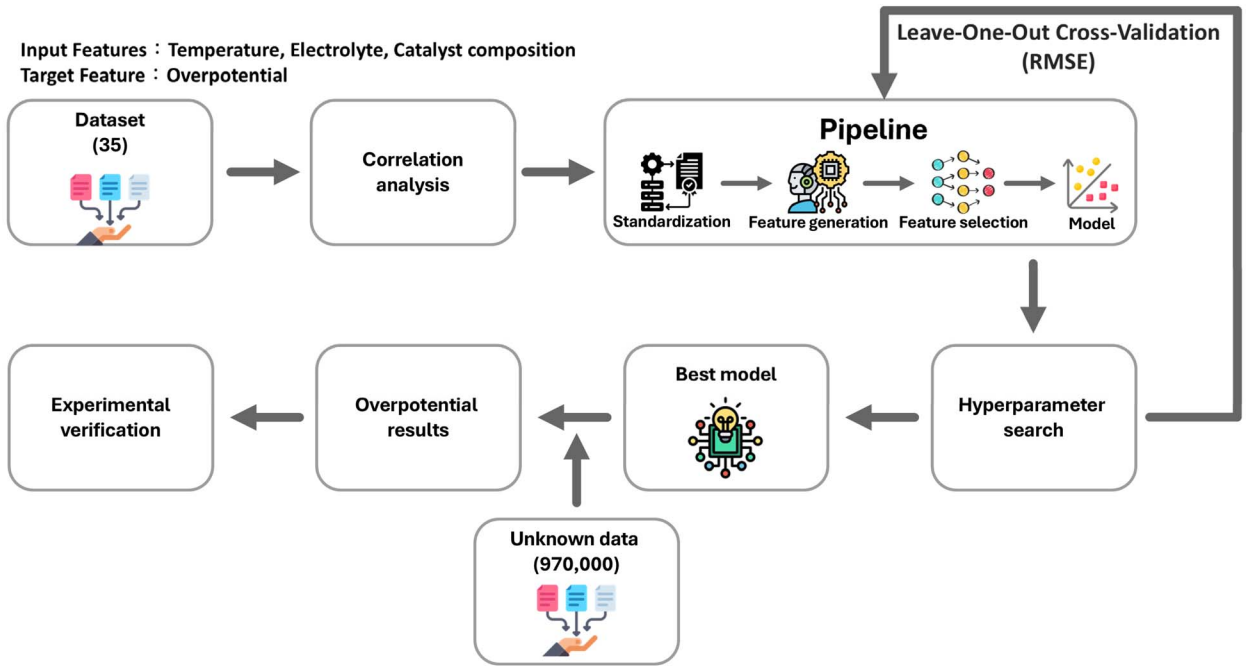

Fig. 1 Workflow of the machine learning optimization.

polynomial regression model. During the construction of the ML model, the four input features, including synthesis temperature, urea concentration, electrolyte concentration, and the molar fractions of catalyst components, were first analyzed concerning the target variable. Subsequently, the data standardization, polynomial feature generation, and feature

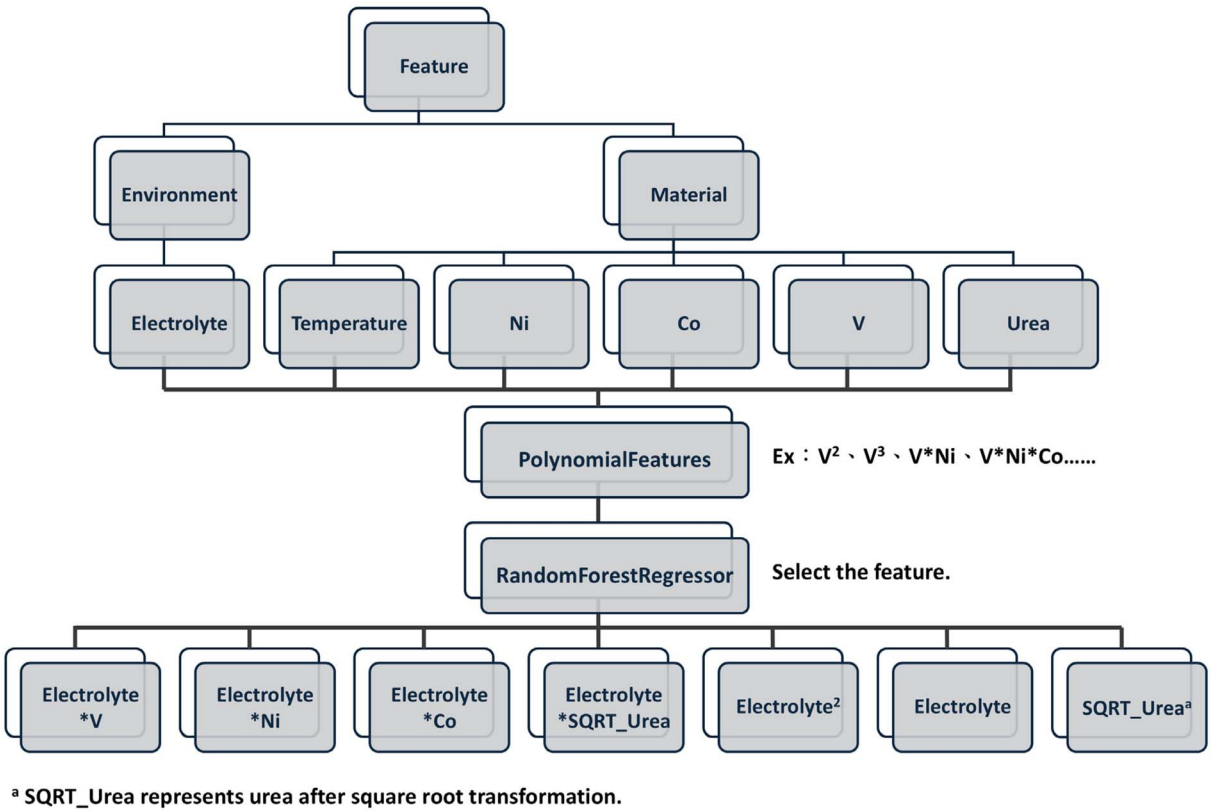

Fig. 2 Feature engineering and selection for polynomial regression model.

selection were performed to train the polynomial regression model. The polynomial regression model was implemented using the scikit-learn library. Besides, the training procedure adopted the grid search method to identify the optimal hyperparameters. Moreover, leave-one-out cross-validation (LOOCV) was utilized to compute the root mean square error (RMSE) for quantitative model performance evaluation. This approach determined the best-performing model and hyperparameters. The ESI materials† provide a detailed explanation of the ML process.

This study aims to optimize the process parameters of OER electrocatalysts to reduce overpotential. First, the correlations between the four input features and the target feature (overpotential) were analyzed. The relationships and correlations between the two features were determined by calculating the Pearson correlation coefficient. Fig. 3a shows the correlation between the input features and the target variable. It can be observed that, from the perspective of overpotential, the highest correlation was 0.38 with temperature, indicating a positive correlation, while the lowest correlation was −0.62 with electrolyte concentration, indicating a negative correlation.

The gradient boosting regression (GBR) algorithm was used to obtain the weights of the input features' influence on the target variable, and a radar chart was generated, as shown in Fig. 3b. It indicated that electrolyte concentration has the highest weight of 74.4%, making it the most influential feature, followed by temperature with 15.8%. From this, it was clear that electrolyte concentration had the most significant influence among the input features, while the impact of the molar fractions of individual metal elements on overpotential is limited. Therefore, based on the training process, it was found that the second-degree polynomial model outperformed the first-degree polynomial (Fig. S4 and S5†). As a result, the final features included interaction terms between the features as inputs to the polynomial regression model.

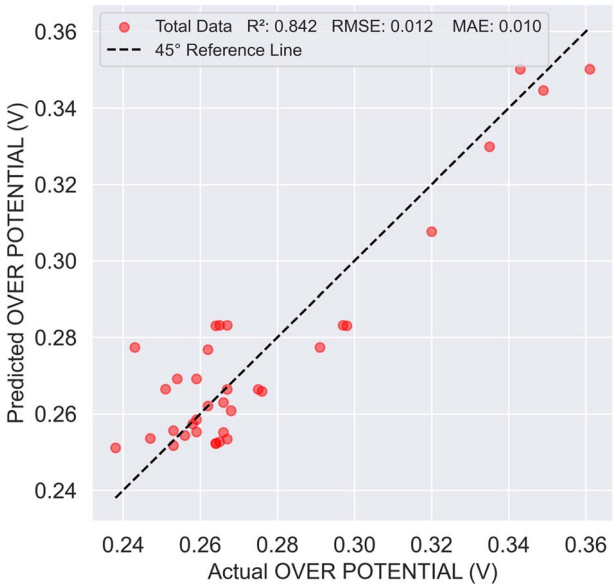

Fig. 4 Scatter plot of predicted OER values and actual overpotential values.

In machine learning, coefficient of determination (R^2), RMSE, and mean absolute error (MAE) were three evaluation metrics used to assess the performance of regression models. Fig. 4 shows the scatter plot of the predicted results *versus* actual overpotentials after training the machine learning model. The closer the data points are to the 45° reference line, the more accurate the model's predictions are. According to the experimental results, the model demonstrated accurate predictive performance, successfully predicting the overpotential with the data points closely aligning with the 45° reference line. The R^2, RMSE, and MAE values were all favorable, with respective values of 0.842, 0.012, and 0.010.

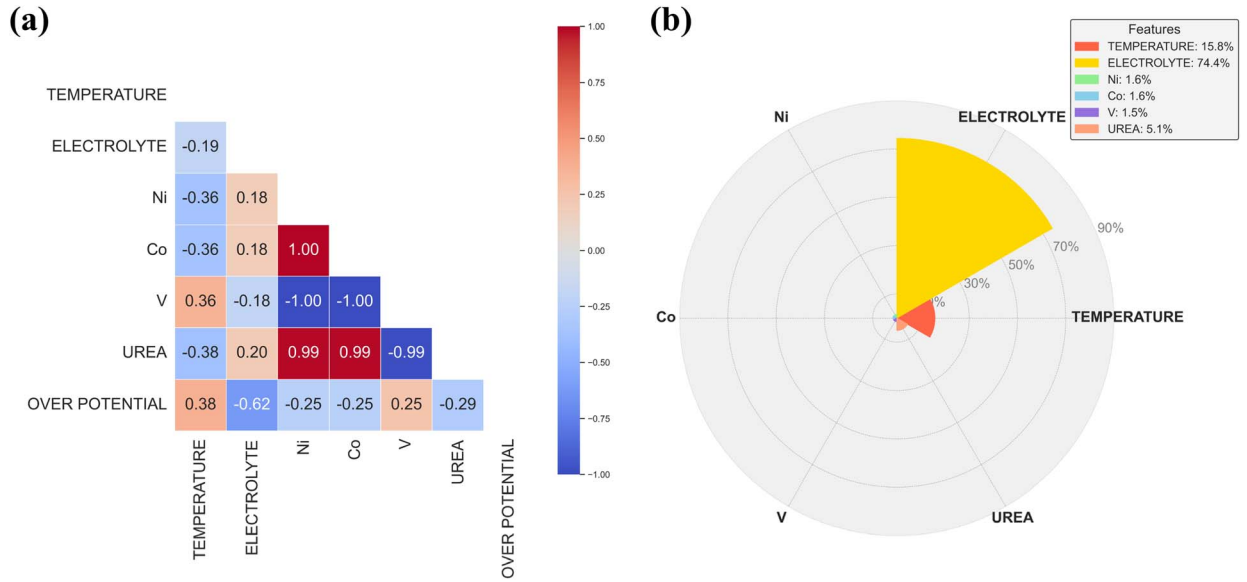

Fig. 3 (a) The correlation coefficient between the input features and target variable, (b) the feature importance predicted by the GBR algorithm.

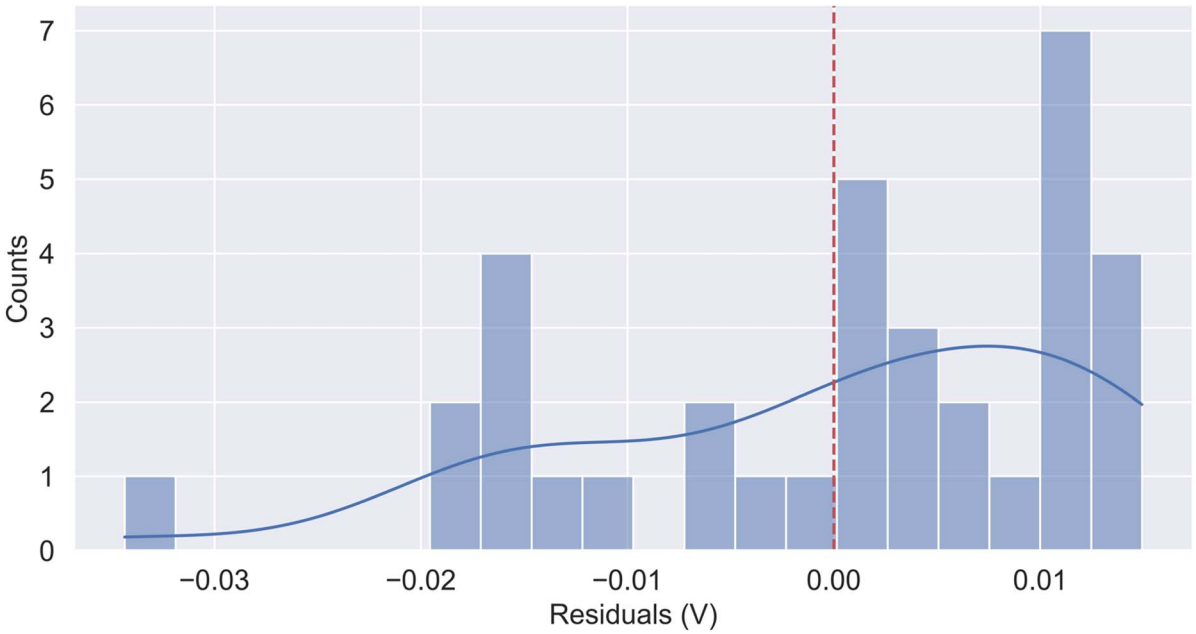

Fig. 5 Residual distribution plot of the best polynomial regression model.

Subsequent calculation of the errors between the actual and predicted values led to the residual distribution shown in Fig. 5. The figure indicates that the majority of the residuals are concentrated between −0.03 V and 0.02 V, with positive residuals slightly higher than the negative residuals, suggesting that the model may slightly underestimate some data points. Overall, the kernel density estimation (KDE) curve indicates that most prediction errors are close to 0, reflecting the model's stable predictive performance.

Shapley additive explanations (SHAP) analysis was conducted on the best model to calculate the importance of input features for the predictive model and to interpret the model's predictions. Fig. 6 presents the average SHAP absolute values for each feature, indicating the overall influence of the features on the model output. It can be observed that the interaction between electrolyte concentration and metal V has the highest average SHAP value, suggesting that it has the strongest impact on the model's predictions. This result aligns well with the

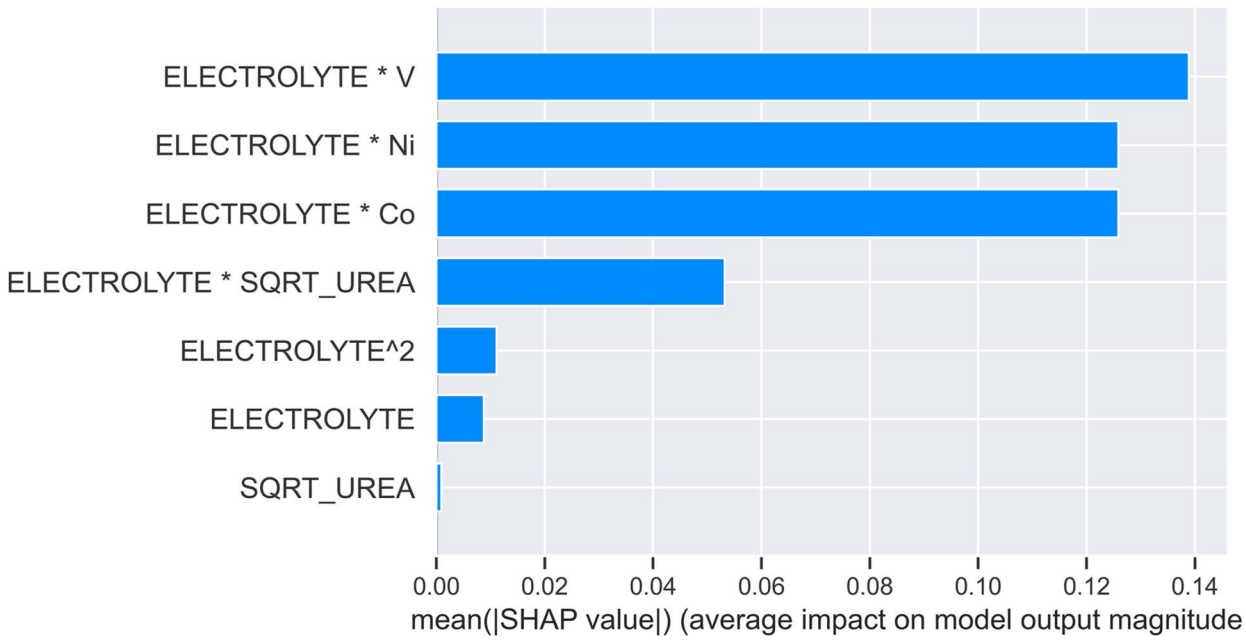

Fig. 6 Bar plot of SHAP values from a polynomial regression model when predicting overpotentials.

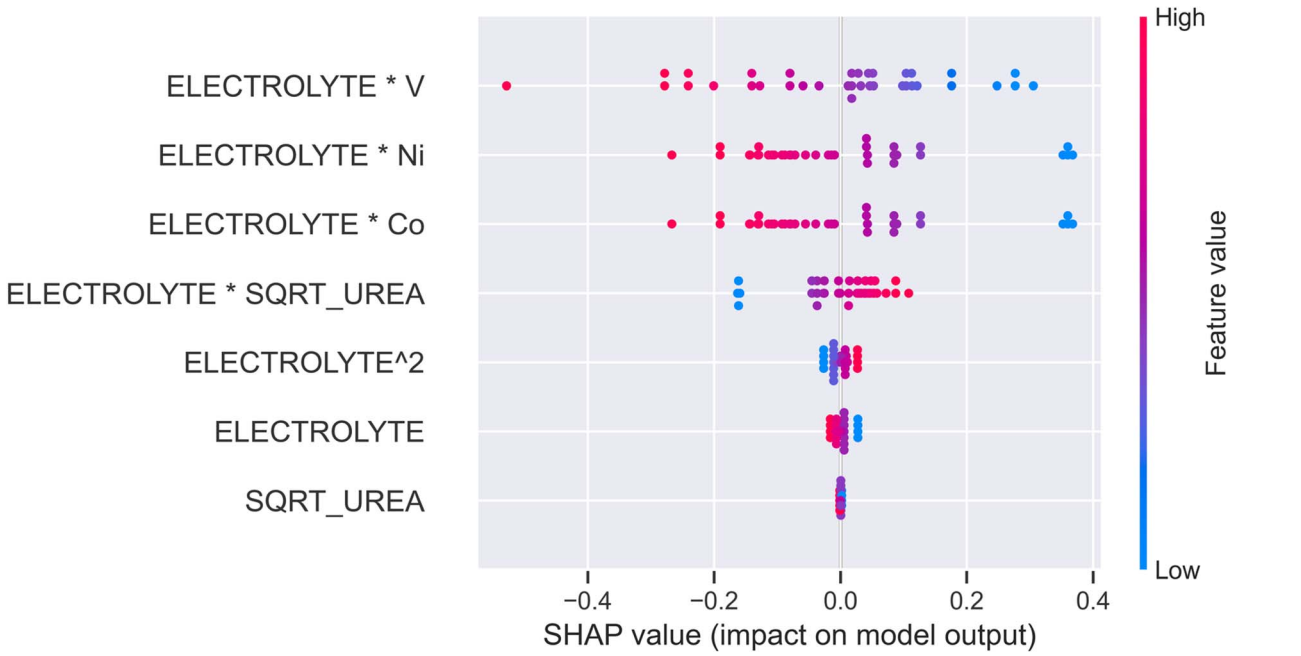

Fig. 7 Beeswarm plot of SHAP values from a polynomial regression model when predicting overpotentials.

study's focus on doping with vanadium to improve overpotential performance. Fig. 7 illustrates how the SHAP values of different features influence the model output. The figure shows that Electrolyte*V, Electrolyte*Ni, and Electrolyte*Co are the most significant features affecting the model output, as evidenced by their wide SHAP value ranges and broad distribution of points.

The study also analyzed the ordinary least squares (OLS) regression results, with Table 1 listing the statistical performance in predicting overpotential. Regarding the p-values, both electrolyte and electrolyte^2 had p-values smaller than 0.05, indicating a significant influence on overpotential. Based on the confidence intervals (CI), electrolyte had a negative effect, whereas electrolyte^2 had a positive effect. Electrolyte*Ni and Electrolyte*Co had p-values ($p = 0.054$) close to the significance threshold ($p = 0.05$), suggesting a potential influence. On the other hand, SQRT_Urea, Electrolyte*V, and Electrolyte*SQRT_Urea had p-values significantly greater than 0.05, indicating a minor impact on overpotential. However, these results were inconsistent with the SHAP analysis mentioned earlier. This discrepancy arose because the molar fractions of the three metal elements were correlated, leading to multicollinearity issues when generating interaction terms, which resulted in variance inflation factor (VIF) values exceeding 10, directly affecting the estimation of each variable's independent influence. Additionally, the regression model assumed a linear relationship between variables, whereas SHAP could capture nonlinear effects. Therefore, the SHAP-based feature importance analysis was considered more reasonable and reliable. After completing model training, a for-loop was employed to automatically generate all possible process parameter combinations within a specific range (approximately 970 000 data). These generated parameters were used for prediction, identifying the optimal process parameters that

Table 1 Statistical analysis of the ML model

Variables	Coefficient	Standard error	t Statistics[a]	P^b ($>t$)	CI[c] (0.025)	CI[d] (0.975)	VIF[e]
Const	3.2029	1.684	1.902	0.067	−0.246	6.652	5.449×10^5
ELECTROLYTE	−0.0485	0.013	−3.692	0.001	−0.075	−0.022	2.350
SQRT_UREA	−0.0087	0.006	−1.354	0.187	−0.022	0.004	1.078
ELECTROLYTE^2	0.0541	0.006	8.757	0.000	0.041	0.067	1.072
ELECTROLYTE*Ni	−1.5289	0.762	−2.007	0.054	−3.089	0.031	Infinity
ELECTROLYTE*Co	−1.5289	0.762	−2.007	0.054	−3.089	0.031	Infinity
ELECTROLYTE*V	−2.8756	1.672	−1.720	0.096	−6.300	0.549	1.761×10^4
ELECTROLYTE*SQRT_UREA	0.1084	0.233	0.466	0.645	−0.368	0.585	3.587×10^2

[a] t Statistic is calculated as the coefficient divided by its standard error. [b] $P(>t)$ represents the p-value of the t-statistic used to test the null hypothesis that the coefficient is zero. A p-value < 0.05 indicates a statistically significant impact on the model. [c] Lower bound of the corresponding confidence interval (2.5th percentile). [d] Upper bound of the corresponding confidence interval (97.5th percentile). [e] VIF is defined as VIF $= (1/(1 - R_i^2))$, where R_i^2 is the coefficient of determination obtained by regressing a given variable against all other variables. If VIF > 10, collinearity issues may exist.

Table 2 The optimal OER process conditions predicted by the ML model and the corresponding experimental data

	Temperature (°C)	Electrolyte (KOH) (M)	Ni	Co	V	Urea (mM)	Overpotential (mV)
Polynomial regression	150	1	0.44	0.44	0.12	5.50	184.024
Experimental verification							196
Experimental dataset[a]	150	0.84	0.44	0.44	0.12	7.30	238

[a] The best overpotential in the initial 35 experimental dataset and the corresponding OER process condition.

yielded the lowest overpotential, as listed in Table 2. Subsequently, experiments were conducted using these parameters to validate the model's feasibility. As a result, the polynomial regression model derived the lowest overpotential value of 184.204 mV, while the experimentally obtained actual overpotential was 196 mV. This value is better than the lowest performance (238 mV) in the training experimental dataset, demonstrating that this ML model can effectively identify the optimal set of process parameters to achieve the best overpotential performance. Fig. 8 compares the overpotentials of the optimized NiCoV LDHs with other OER electrocatalysts developed using the ML algorithm in the literature.[36,37,41,43–47] It is found that the optimized NiCoV LDHs performs better with an overpotential of 196 mV lower than that of $Ni_{0.77}Fe_{0.13}La_{0.1}$ (226 mV)[41] and $Co_{2.5}Ga_{0.5}O_4$ (220 mV),[44] confirming again the effectiveness of the ML algorithm developed in this work.

2.3. Structural and chemical characterization of optimized electrocatalyst

NiCoV LDHs was successfully synthesized using the hydrothermal method described in ESI,† wherein the material composition and urea concentration were optimized as shown in Table 2. The morphological and crystallographic characteristics of the synthesized catalyst were analyzed using scanning electron microscopy (SEM) and transmission electron microscopy (TEM). From the SEM image (Fig. 9a), the catalyst reveals a stacked sheet-like structure, indicating the typical layered morphology of LDHs. This observation is further corroborated by TEM analysis (Fig. 9b and c), which clearly displays the sheet-like arrangement, confirming the layered nature of the synthesized LDHs. Additionally, the high-resolution TEM image (inset in Fig. 9b) show well-defined lattice fringes with an interplanar spacing of 0.196 nm, which corresponds to the (018) plane, further validating the crystalline nature. Furthermore, elemental distribution was examined through energy dispersive X-ray spectroscopy (EDX) mapping (Fig. 10), which confirms the uniform presence of Ni, Co, and V, verifying the successful incorporation of these elements into the LDHs structure. These combined results strongly support the successful synthesis of NiCoV LDHs with a well-defined layered morphology and homogeneous elemental distribution.

The crystalline nature of the synthesized NiCoV LDHs was further confirmed through X-ray diffraction (XRD) analysis. The XRD pattern (Fig. 9d) exhibits distinct diffraction peaks at 11.4°, 23.6°, 34.01°, 39.8°, 46.08°, 60.84°, and 63.12°, which correspond to the (003), (006), (012), (015), (018), (010), and (013) lattice planes, respectively. These diffraction peaks are characteristic of LDHs and closely match the standard reference

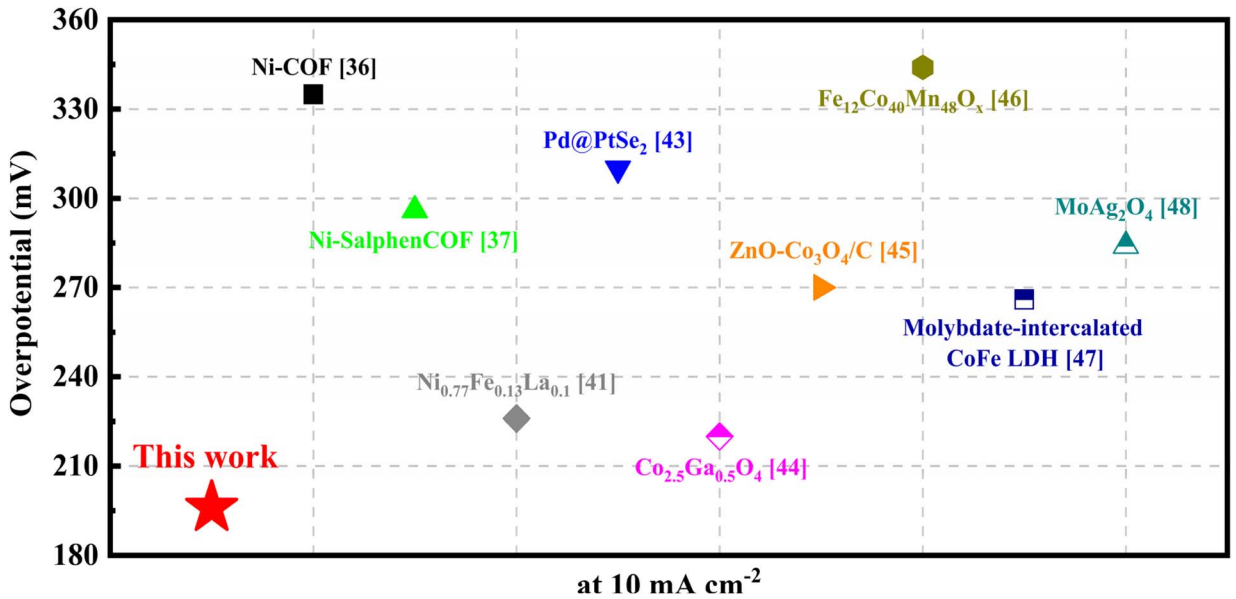

Fig. 8 The comparison of the overpotential of the NiCoV LDHs with those of recently reported electrocatalysts at 10 mA cm^{-2}.[36,37,41,43–48]

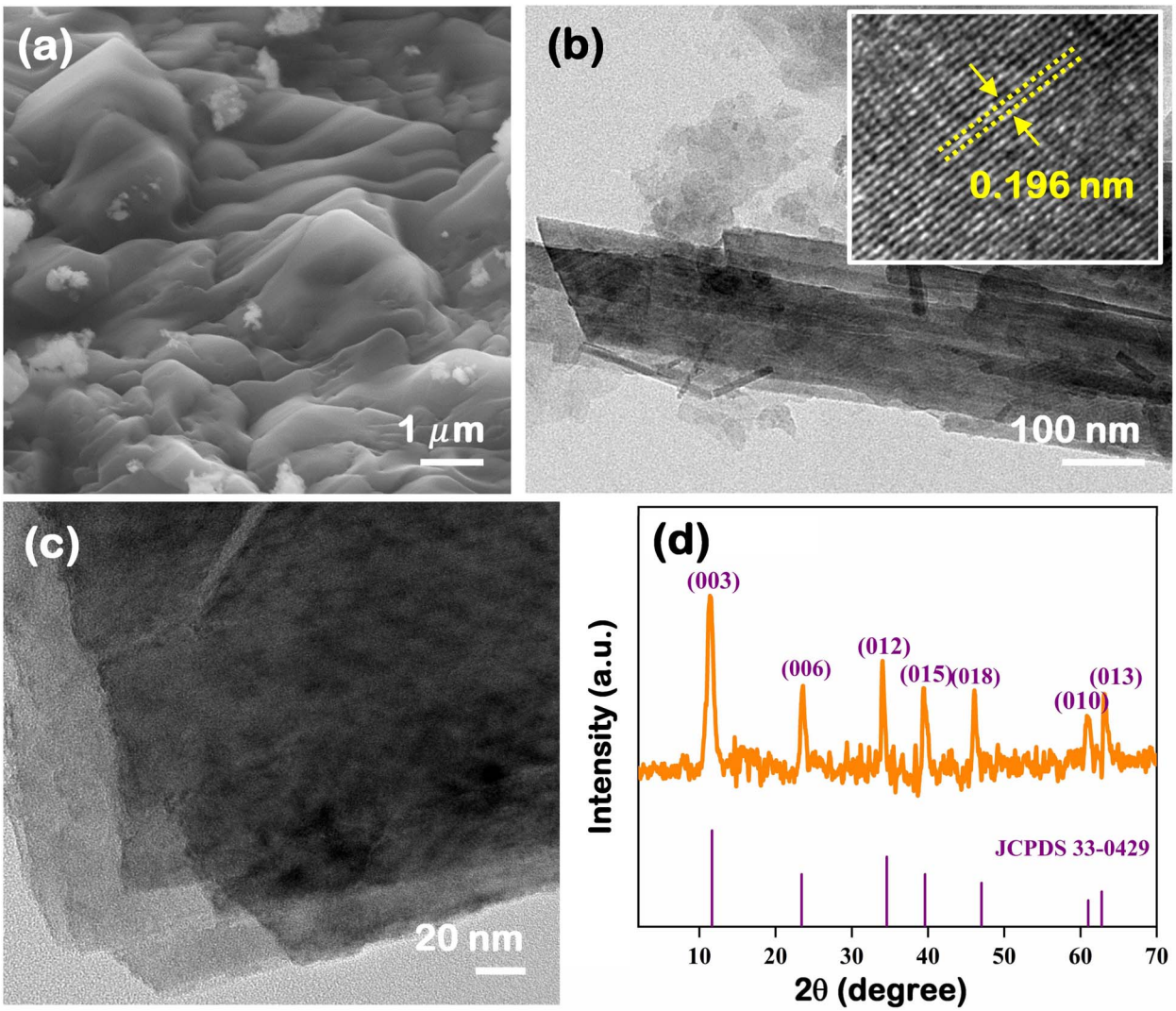

Fig. 9 Morphological and structural characterization of NiCoV LDHs: (a) SEM image, (b) TEM image (low magnification with an inset of SAED pattern), (c) TEM image (high magnification), (d) XRD pattern.

pattern JCPDS 33-0429, confirming the successful formation of the LDHs phase.[49] The presence of the (003) and (006) reflections at lower angles indicates the well-defined stacking of the layered structure, which is a typical feature of LDHs. The higher-angle peaks, such as (018), (010), and (013), further validate the ordered arrangement and crystallinity of the material. These findings, in conjunction with morphological analysis, provide strong evidence for the successful synthesis of NiCoV LDHs with a well-structured layered architecture.

The physicochemical properties of the synthesized NiCoV LDHs were examined through Brunauer–Emmett–Teller (BET) surface area analysis and X-ray photoelectron spectroscopy (XPS). The BET analysis (Fig. S7, ESI†) reveals that the specific surface area of NiCoV LDHs is approximately 25.8 m^2 g^{-1}, indicating a moderate surface area that is beneficial for catalytic and electrochemical applications, particularly in OER and related energy conversion process. First, the NiCoV LDHs catalyst, composed of 45.05 wt% Ni, 42.86 wt% Co, and 12.09 wt% V (as determined by inductively coupled plasma optical emission spectroscopy, ICP-OES), was synthesized *via* hydrothermal treatment using optimized precursor ratios (Fig. S8, ESI†). To gain deeper insight into the elemental composition and oxidation states of the elements present in NiCoV LDHs, XPS analysis was performed. The survey spectrum confirms the presence of Ni, Co, V, and O, with high-resolution deconvolution providing detailed information on their oxidation states.

The Ni 2p spectrum (Fig. 11a) shows two main peaks at 855 eV and 872.8 eV, corresponding to Ni $2p_{3/2}$ and Ni $2p_{1/2}$, respectively. Deconvolution of the Ni $2p_{3/2}$ peak reveals two distinct components at 854.8 eV and 856.8 eV, which are assigned to Ni^{2+} and Ni^{3+}, respectively. Satellite peaks are observed at 861.0 eV and 879.0 eV, characteristic of the Ni^{2+} oxidation state. The deconvolution was carried out using a Gaussian–Lorentzian (GL(30)) function, with the full width at half maximum (FWHM) fixed at 1.5 eV for main peaks and

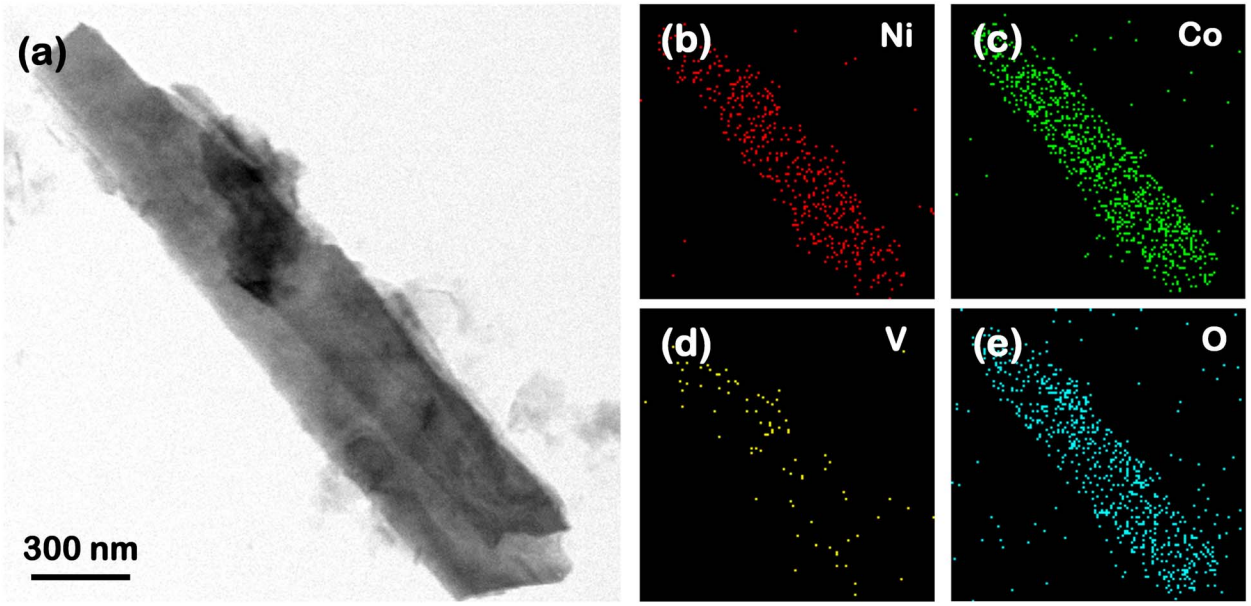

Fig. 10 (a) TEM image of sheet-like NiCoV LDHs and its corresponding EDX elemental mapping of (b) Ni, (c) Co, (d) V, and (e) O.

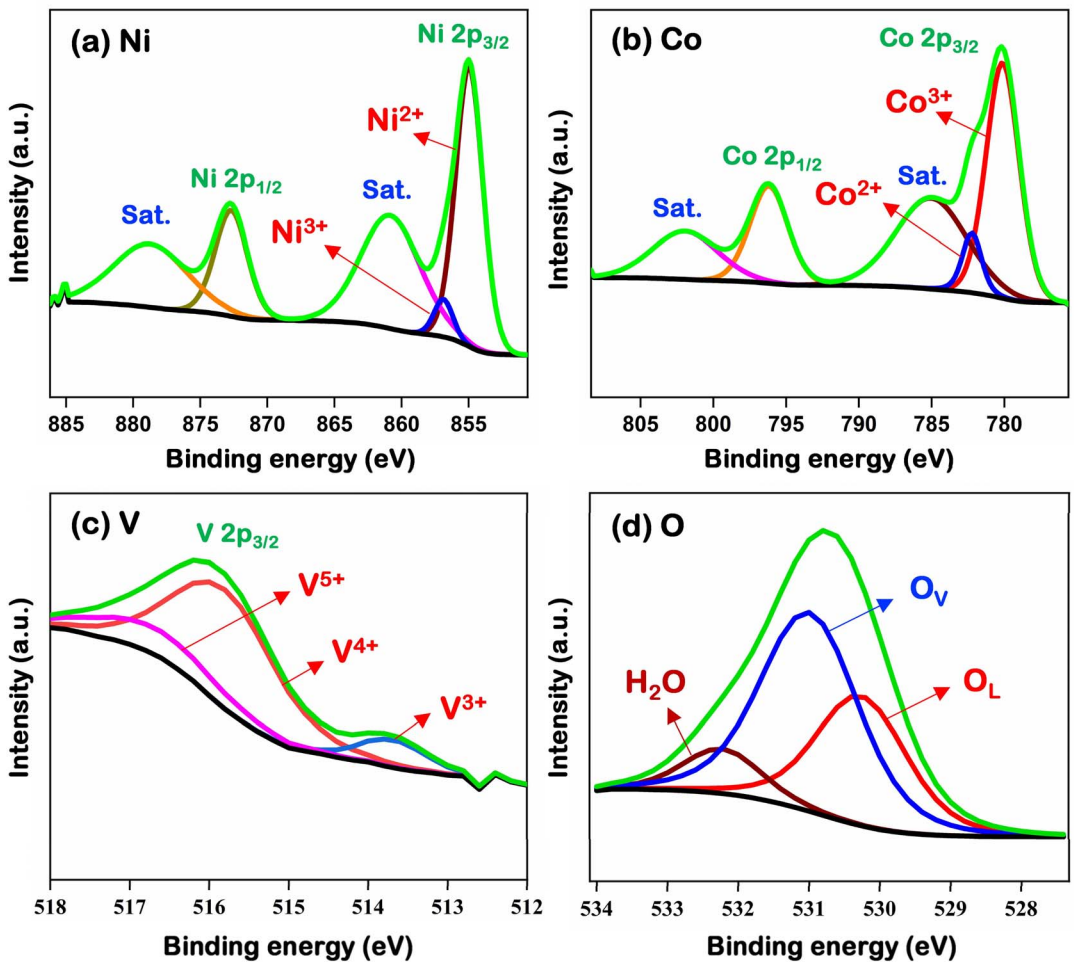

Fig. 11 XPS Spectra of (a) Ni 2p, (b) Co 2p, (c) V 2p, and (d) O 1s of NiCoV LDHs.

3.0 eV for satellite peaks.[50,51] Similarly, the Co 2p spectrum (Fig. 11b) displays two main peaks at 780.2 eV and 796.2 eV, corresponding to Co $2p_{3/2}$ and Co $2p_{1/2}$. The Co $2p_{3/2}$ region was deconvoluted into two peaks at 780.2 eV (Co^{3+}) and 782.2 eV (Co^{2+}). Corresponding satellite peaks at 785.0 eV and 802 eV further confirm the presence of Co^{2+} species. The fitting protocol followed the same GL (30) profile with fixed FWHM as used for Ni.[52,53] The V 2p spectrum (Fig. 11c) shows a primary peak at 516.0 eV, corresponding to V $2p_{3/2}$. Further deconvolution of this peak identified three components at 513.8 eV, 516.0 eV, and 516.8 eV, which can be assigned to V^{3+}, V^{4+}, and V^{5+}, respectively. The presence of multiple oxidation states of vanadium suggests its role in facilitating redox activity, which is essential for electrochemical applications.[24]

The O 1 s spectrum (Fig. 11d) was analyzed to understand the different oxygen species present in the NiCoV LDHs. The main peak at 530.8 eV was deconvoluted into three distinct components: 530.2 eV, associated with lattice oxygen (O_L), 531.0 eV corresponding to oxygen vacancy (O_V), and 532.2 eV, attributed to adsorbed water (H_2O).[54,55] A comparative analysis of the O 1s region for NiCoV (Fig. 11d) and NiCo LDHs (Fig. S9, ESI†) reveals significant differences in the oxygen vacancy content. The calculated oxygen vacancy ratios were 0.34 for NiCo and 0.41 for NiCoV LDHs, indicating that a greater proportion of oxygen vacancy in the NiCoV LDHs. The higher oxygen vacancy ratio in NiCoV LDHs not only confirms the successful modification of the catalyst surface but also supports the notion that the enhanced activity of NiCoV LDHs arises from its ability to follow the lattice oxygen mechanism. The presence of oxygen vacancies improves the electronic conductivity and facilitates the adsorption and desorption of oxygen intermediates in LOM, thereby accelerating the OER process.[54,55] Furthermore, the mixed oxidation states of Ni, Co, and V, along with the presence of oxygen vacancies, create a favorable electronic environment for charge transfer. This synergistic effect enhances the intrinsic activity of the catalyst, making NiCoV LDHs a promising material for electrocatalytic applications, particularly in energy storage and conversion technologies.

2.4. Electrochemical performance of optimized electrocatalyst

The four feature variables detailed in Table 2 were meticulously refined to minimize the overpotential essential for the OER on the electrocatalyst. The composite material was synthesized with precisely calibrated concentrations of NiCoV LDHs/NF, temperature, and KOH concentration. The optimization process projected an overpotential of 184 mV under optimal conditions (Table 2). Experimental validation revealed an overpotential of 196 mV (Fig. 12a), reflecting a minor deviation of 6.1% from the predicted value. This strong concordance between the experimental and predicted results demonstrates the efficacy and reliability of the model in fine-tuning the variables for optimal overpotential reduction. The electrochemical activity of the optimized NiCoV LDHs/NF electrode, was investigated through linear sweep voltammetry (LSV) under carefully optimized conditions. These conditions include a KOH concentration of 1 M and a scan rate of 10 mV s^{-1}. To evaluate the intrinsic contribution of the nickel foam (NF) substrate to the OER performance, a control experiment using bare NF was conducted under the same electrochemical conditions. The bare NF required an overpotential of 318 mV to reach a current density of 10 mA cm^{-2}, which is significantly higher than that of the optimized NiCoV LDHs/NF electrode (196 mV). This confirms that the improved electrocatalytic activity is attributed primarily to the NiCoV LDHs catalyst, rather than the substrate itself. The comparative LSV curve of bare NF is provided in the ESI (Fig. S10, ESI†).

Additionally, the inset in Fig. 12a displays the Tafel plot derived from the LSV data, offering a detailed analysis of the electrode's performance. To ensure the reliability of the results, the potential values derived from the LSV tests were calibrated against the reversible hydrogen electrode (RHE). The optimized

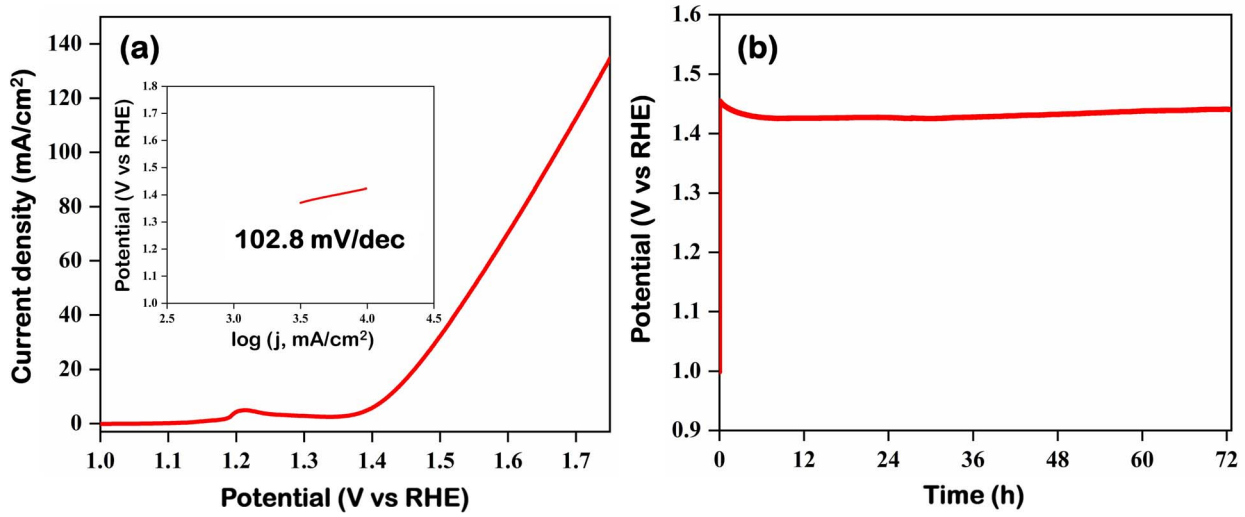

Fig. 12 (a) LSV curve and (b) chronopotentiometry curve of optimized NiCoV LDHs (inset in (a) is Tafel plot).

conditions consistently yield a significantly lower overpotential and a notably higher limiting current density. These observations underscore the substantial enhancement in OER catalytic activity achieved through parameter optimization. This advancement marks a critical step forward in advancing the understanding and practical application of NiCoV LDHs/NF electrocatalysts for the OER. The Tafel slope for the optimized NiCoV LDHs was measured to be 102.8 mV dec^{-1}. Since a lower Tafel slope generally indicates faster reaction kinetics, this result reinforces the superior catalytic activity of NiCoV LDHs for the OER application. This faster kinetic response is crucial for practical energy conversion systems, as it directly contributes to improved efficiency and reduced energy losses.

The stability and reusability of the optimized electrode were assessed using chronopotentiometry testing. Beyond its impressive electrocatalytic activity, the composite electrocatalyst showcased excellent durability for the OER. As depicted in Fig. 12b, the catalyst maintained consistent performance over 72 h of continuous operation at a current density of 10 mA cm^{-2}, highlighting its robust and reliable performance under prolonged testing conditions. The remarkable stability and durability observed provide strong evidence of the catalyst's potential for reuse under identical conditions. This robustness can be attributed to the abundance of catalytically active sites and the presence of oxygen vacancies, which together enhance the catalyst's resilience during the OER. These synergistic factors play a pivotal role in improving the material's overall stability and performance.

In addition, the impact of electrical conductivity on OER performance was examined using electrochemical impedance spectroscopy (EIS). The resulting Nyquist plots (Fig. S11, ESI†) and the corresponding equivalent circuit (including the charge transfer resistance, R_{ct}, shown in Fig. S12, ESI†) provide further insight into the interfacial properties between the catalysts and electrolytes. Remarkably, NiCoV LDHs exhibits an exceptionally low charge transfer resistance of 19.2 Ω. This minimal interfacial resistance facilitates rapid and efficient electron transfer during the OER process, which is critical for enhancing overall catalytic performance and stability in practical applications. Together, the favorable Tafel kinetics and low R_{ct} underscore

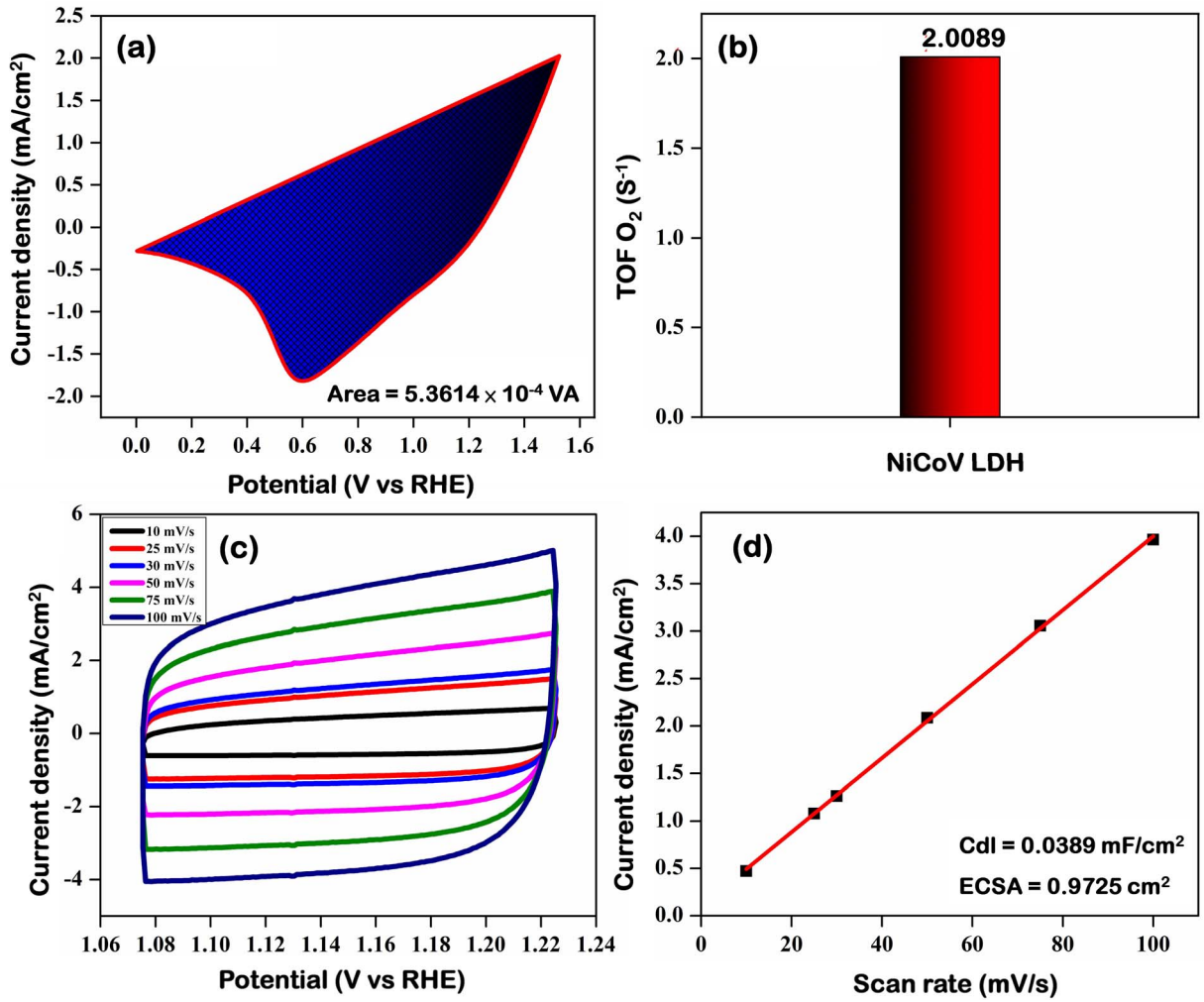

Fig. 13 Electrochemical characterization of optimized NiCoV LDHs: (a) area of reduction peak, (b) TOF value at 300 mV, (c) CV curves at different scan rates, (d) linear fit of current density *vs.* scan rates.

the potential of NiCoV LDHs as highly effective electrocatalysts for oxygen evolution, offering significant advantages for sustainable energy conversion technologies.

The redox-active surface area of the NiCoV LDHs catalyst was determined by focusing on the reduction peaks and excluding the corresponding oxidation peaks of the redox couple.[56] As illustrated in Fig. 13a, the calculated value was 5.3614×10^{-4} VA. The result clearly indicates that NiCoV LDHs possesses a greater number of accessible redox-active sites, which directly contributes to its superior performance in the OER. Furthermore, turnover frequency (TOF) analysis was conducted using the redox area curve at a fixed potential of 300 mV. The derived TOF value, presented in the bar chart in Fig. 13b, underscores that NiCoV LDHs exhibits significantly enhanced OER activity, achieving a TOF value of 2.0089 s^{-1}. Detailed methodologies for the TOF calculations are provided in the ESI.†

The double layer capacitance (C_{dl}) was used to evaluate the electrochemical surface area (ECSA) of the optimized sample. The cyclic voltammetry (CV) curves, recorded at various scan rates, are depicted in Fig. 13c. Notably, the NiCoV LDHs exhibited the C_{dl} value of 0.0389 mF cm^{-2}, corresponding to an ECSA of 0.9725 cm^2 (Fig. 13d). This larger ECSA is particularly important because it indicates a greater number of active sites available for electrochemical reactions, which can lead to enhanced catalytic performance. The increased active surface area not only improves electron transfer kinetics but also underpins the material's potential in energy conversion and storage applications.

3 Conclusions

This work demonstrates a successful integration of ML optimization with experimental datasets to develop a high-performance NiCoV LDHs electrocatalyst coupled with optimized electrolyte concentration and synthesis temperature for improved OER. By systematically varying key process parameters (input features such as catalyst composition, electrolyte concentration, and synthesis temperature), the trained ML model accurately predicted an optimal overpotential (target feature) of 184 mV, which was better than the lowest value of 238 mV in the original training experimental datasets. Further experimental verification based on the optimized input features produced an overpotential of 196 mV, confirming the high accuracy of the ML algorithm. Notably, the ML analysis showed that the interplay between the electrolyte concentration and vanadium doping played a key role in determining the overpotential. XPS results further confirmed that the incorporation of vanadium in the NiCoV LDHs enhanced the availability of lattice oxygen, thereby achieving more efficient OER through the LOM mechanism. The optimized catalyst exhibited a Tafel slope of 102.8 mV dec^{-1}, indicating fast reaction kinetics, alongside an ECSA of 0.9725 cm^2 and a TOF of 2.0089 s^{-1}, both of which confirmed the enhanced availability of active sites and intrinsic catalytic efficiency. Detailed morphological and chemical characterizations further corroborated the improved structural integrity and enhanced lattice oxygen content due to vanadium doping. Long-term stability testing proved that the optimized catalyst maintained stable electrocatalytic performance over 72 h. Overall, these findings validate the effectiveness of the ML-assisted approach in guiding the synthesis of efficient electrocatalysts and pave the way for further development of advanced materials for sustainable energy applications.

Data availability

The data supporting this article have been already included in the main text or/and as part of the ESI.†

Author contributions

Chandrasekaran Pitchai: methodology, validation, formal analysis, visualization, investigation, writing – original draft. Ting-Yu Lo: methodology, software, validation, formal analysis, investigation, data curation, visualization, writing – original draft. Hou-Chien Chang: formal analysis, resources. Hung-Chung Li: conceptualization, software, supervision, data curation, writing - review & editing. Ming-Der Yang: conceptualization, supervision, funding acquisition, writing - review & editing. Chih-Ming Chen: conceptualization, investigation, resources, supervision, funding acquisition, writing - review & editing.

Conflicts of interest

The authors declare no competing financial interest.

Acknowledgements

The authors appreciate the financial support from the National Science and Technology Council, Taiwan through Grants NSTC 113-2634-F-005-002, NSTC 113-2811-E-005-010-MY3 and NSTC 113-2221-E-005-007-MY3. Many thanks also go to the financial support from the "Innovation and Development Center of Sustainable Agriculture" from The Featured Areas Research Center Program within the framework of the Higher Education Sprout Project by the Ministry of Education (MOE) in Taiwan.

References

1 E. Mahmoudi, E. Asghari, N. Delibaş and A. Niaei, *Sci. Rep.*, 2023, **13**, 22878.
2 R. Khan, M. T. Mehran, S. R. Naqvi, A. H. Khoja, K. Mahmood, F. Shahzad and S. Hussain, *Int. J. Energy Res.*, 2020, **44**, 9714–9747.
3 M.-D. Yang, M.-D. Lin, Y.-H. Lin and K.-T. Tsai, *Appl. Therm. Eng.*, 2017, **111**, 1255–1264.
4 Y.-H. Lin, K.-T. Tsai, M.-D. Lin and M.-D. Yang, *Appl. Energy*, 2016, **171**, 336–346.
5 P. Chandrasekaran, T. N. J. I. Edison and M. G. Sethuraman, *Fuel*, 2022, **320**, 123947.
6 P. Chandrasekaran, T. N. J. I. Edison and M. G. Sethuraman, *Int. J. Hydrogen Energy*, 2020, **45**, 28800–28811.
7 X. F. Lu, Y. Chen, S. Wang, S. Gao and X. W. Lou, *Adv. Mater.*, 2019, **31**, 1902339.

8 S. Anantharaj, S. R. Ede, K. Karthick, S. Sam Sankar, K. Sangeetha, P. E. Karthik and S. Kundu, *Energy Environ. Sci.*, 2018, **11**, 744–771.
9 Y. Yao, J. Lyu, X. Li, C. Chen, F. Verpoort, J. Wang, Z. Pan and Z. Kou, *DeCarbon*, 2024, **5**, 100062.
10 W. Sang, K. Liu, T. Wang, J. Lyu, Z. Nie, L. Zhang, M. Xiong, X. Li, L. Zheng, C. Chen and F. Verpoort, *Nano Energy*, 2025, **138**, 110861.
11 M. Tahir, L. Pan, F. Idrees, X. Zhang, L. Wang, J.-J. Zou and Z. L. Wang, *Nano Energy*, 2017, **37**, 136–157.
12 T. Audichon, T. W. Napporn, C. Canaff, C. Morais, C. Comminges and K. B. Kokoh, *J. Phys. Chem. C*, 2016, **120**, 2562–2573.
13 B. Jiang, J. Zhu, Z. Xia, J. Lyu, X. Li, L. Zheng, C. Chen, S. Chaemchuen, T. Bu, F. Verpoort and S. Mu, *Adv. Mater.*, 2024, **2**, 2310699.
14 J. Chen, G. Fu, Y. Tian, X. Li, M. Luo, X. Wei, T. Zhang, T. Gao, C. Chen, S. Chaemchuen and X. Xu, *Interdiscip. Mater.*, 2024, **4**, 595–606.
15 O. Kasian, J. P. Grote, S. Geiger, S. Cherevko and K. J. Mayrhofer, *Angew. Chem., Int. Ed.*, 2018, **57**, 2488–2491.
16 X. Li, X. Hao, A. Abudula and G. Guan, *J. Mater. Chem. A*, 2016, **4**, 11973–12000.
17 A. Karmakar, K. Karthick, S. S. Sankar, S. Kumaravel, R. Madhu and S. Kundu, *J. Mater. Chem. A*, 2021, **9**, 1314–1352.
18 C. Pitchai, S. M. Gopalakrishnan and C.-M. Chen, *Energy Fuels*, 2024, **38**, 2235–2247.
19 X. Ge, C. Gu, X. Wang and J. Tu, *J. Mater. Chem. A*, 2014, **2**, 17066–17076.
20 S. Yin, W. Tu, Y. Sheng, Y. Du, M. Kraft, A. Borgna and R. Xu, *Adv. Mater.*, 2018, **30**, 1705106.
21 J. Liu, J. Wang, B. Zhang, Y. Ruan, L. Lv, X. Ji, K. Xu, L. Miao and J. Jiang, *ACS Appl. Mater. Interfaces*, 2017, **9**, 15364–15372.
22 K. Bera, A. Karmakar, S. Kumaravel, S. Sam Sankar, R. Madhu, H. N. Dhandapani, S. Nagappan and S. Kundu, *Inorg. Chem.*, 2022, **61**, 4502–4512.
23 J. Wang, Y. Sun, Y. Qi and C. Wang, *ACS Appl. Mater. Interfaces*, 2021, **13**, 57392–57402.
24 D. He, L. Cao, J. Huang, Y. Feng, G. Li, D. Yang, Q. Huang and L. Feng, *ACS Sustainable Chem. Eng.*, 2021, **9**, 12005–12016.
25 G. L. Hart, T. Mueller, C. Toher and S. Curtarolo, *Nat. Rev. Mater.*, 2021, **6**, 730–755.
26 J. Wei, X. Chu, X.-Y. Sun, K. Xu, H.-X. Deng, J. Chen, Z. Wei and M. Lei, *InfoMat*, 2019, **1**, 338–358.
27 H. Mai, T. C. Le, D. Chen, D. A. Winkler and R. A. Caruso, *Chem. Rev.*, 2022, **122**, 13478–13515.
28 M.-D. Yang, Y.-C. Hsu, W.-C. Tseng, H.-H. Tseng and M.-H. Lai, *Comput. Electron. Agric.*, 2025, **230**, 109813.
29 Y. B. Kebede, M.-D. Yang and C.-W. Huang, *Eng. Appl. Artif. Intell.*, 2024, **135**, 108870.
30 M.-D. Yang, Y.-C. Hsu, T.-T. Liu and H.-H. Huang, *Comput. Electron. Agric.*, 2025, **231**, 110058.
31 J. Li, N. Wu, J. Zhang, H.-H. Wu, K. Pan, Y. Wang, G. Liu, X. Liu, Z. Yao and Q. Zhang, *Nano-Micro Lett.*, 2023, **15**, 227.
32 T. Liu, X. Zhao, X. Liu, W. Xiao, Z. Luo, W. Wang, Y. Zhang and J.-C. Liu, *J. Energy Chem.*, 2023, **81**, 93–100.
33 L. Chen, X. Zhang, A. Chen, S. Yao, X. Hu and Z. Zhou, *Chin. J. Catal.*, 2022, **43**, 11–32.
34 N. Ma, Y. Zhang, Y. Wang, C. Huang, J. Zhao, B. Liang and J. Fan, *Appl. Surf. Sci.*, 2023, **628**, 157225.
35 S. Cao, Y. Luo, T. Li, J. Li, L. Wu and G. Liu, *Mol. Catal.*, 2023, **551**, 113625.
36 W. Zhou, L. Yang, X. Wang, W. Zhao, J. Yang, D. Zhai, L. Sun and W. Deng, *JACS Au*, 2021, **1**, 1497–1505.
37 Z. Zhang, Z. Zhang, C. Chen, R. Xu, X.-B. Chen, H. Lu, Z. Shi, Y. Han and S. Feng, *Adv. Mater.*, 2024, **36**, 2403549.
38 C. Andronescu, S. Seisel, P. Wilde, S. Barwe, J. Masa, Y.-T. Chen, E. Ventosa and W. Schuhmann, *Chem.–Eur. J.*, 2018, **24**, 13773–13777.
39 M. M. Silva, R. A. Raimundo, T. R. Silva, A. J. Araújo, D. A. Macedo, M. A. Morales, C. P. Souza, A. G. Santos and A. L. Lopes-Moriyama, *J. Electroanal. Chem.*, 2023, **933**, 117277.
40 G. C. da Silva, N. Perini and E. A. Ticianelli, *Appl. Catal. B: Environ.*, 2017, **218**, 287–297.
41 X. Jiang, Y. Wang, B. Jia, X. Qu and M. Qin, *ACS Appl. Mater. Interfaces*, 2022, **14**, 41141–41148.
42 A. Zheng, Y. Wang, F. Zhang, C. He, S. Zhu and N. Zhao, *iScience*, 2021, **24**, 103430.
43 S. Yue, D. Li, A. Zhang, Y. Yan, H. Yan, Z. Feng and W. Wang, *J. Mater. Chem. A*, 2024, **12**, 5451–5463.
44 S. G. H. Kumar, C. Bozal-Ginesta, N. Wang, J. Abed, C. H. Shan, Z. Yao and A. Aspuru-Guzik, *Chem. Sci.*, 2024, **15**, 10556–10570.
45 F. Zafar, M. Asad, W. Sajjad, M. A. Khan, N. Akhtar, S. U. Hassan and C. Yu, *Int. J. Hydrogen Energy*, 2025, **98**, 384–393.
46 L. Zhang, J. Hou, H. Ji, D. Meng, J. Qi and X. San, *Catalysts*, 2024, **14**, 513.
47 C. Y. J. Lim, R. I. Made, Z. H. J. Khoo, C. K. Ng, Y. Bai, J. Wang, G. Yang, A. D. Handoko and Y.-F. Lim, *Mater. Horiz.*, 2023, **10**, 5022–5031.
48 Y. Li, X. Zhang, T. Li, Y. Chen, Y. Liu and L. Feng, *J. Mater. Chem. A*, 2024, **12**, 19362–19377.
49 Z. Wu, D. Khalafallah, C. Teng, X. Wang, Q. Zou, J. Chen, M. Zhi and Z. Hong, *J. Alloys Compd.*, 2020, **838**, 155604.
50 H. Y. Wang, Y. Y. Hsu, R. Chen, T. S. Chan, H. M. Chen and B. Liu, *Adv. Energy Mater.*, 2015, **5**, 1500091.
51 J. Jiang, A. Zhang, L. Li and L. Ai, *J. Power Sources*, 2015, **278**, 445–451.
52 T. Guan, L. Fang, L. Liu, F. Wu, Y. Lu, H. Luo, J. Hu, B. Hu and M. Zhou, *J. Alloys Compd.*, 2019, **799**, 521–528.
53 C. Yuan, J. Li, L. Hou, X. Zhang, L. Shen and X. W. Lou, *Adv. Funct. Mater.*, 2012, **22**, 4592–4597.
54 J. Li, L. Wang, H. He, Y. Chen, Z. Gao, N. Ma, B. Wang, L. Zheng, R. Li, Y. Wei, J. Xu, Y. Xu, B. Cheng, Z. Yin and D. Ma, *Nano Res.*, 2022, **15**, 4986–4995.
55 Y.-H. Wang, L. Li, J. Shi, M.-Y. Xie, J. Nie, G.-F. Huang, B. Li, W. Hu, A. Pan and W.-Q. Huang, *Adv. Sci.*, 2023, **10**, 2303321.
56 C. Pitchai and C. M. Chen, *Sust. Energy Fuels*, 2025, **9**, 1829–1838.